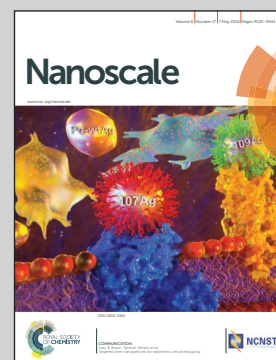


Showcasing work from the Department of Materials Science and Engineering, Korea Advanced Institute of Science and Technology (KAIST), and the Departments of Chemical Engineering and Materials Science & Engineering, Massachusetts Institute of Technology.

Title: Coaxial electrospinning of  $\text{WO}_3$  nanotubes functionalized with bio-inspired Pd catalysts and their superior hydrogen sensing performance

This work introduces macroporous  $\text{WO}_3$  nanotubes (NTs) functionalized with nanoscale catalysts for high performance chemical sensors. Dramatically improved hydrogen sensing properties such as a high response and a fast responding speed were achieved using a highly porous nanotubular structure with well-dispersed nanoscale catalysts assisted by polystyrene colloid templates and protein-encapsulated Pd NPs.

As featured in:



See Gregory C. Rutledge, Il-Doo Kim *et al.* *Nanoscale*, 2016, 8, 9159.



[www.rsc.org/nanoscale](http://www.rsc.org/nanoscale)

Registered charity number: 207890



Cite this: *Nanoscale*, 2016, **8**, 9159

## Coaxial electrospinning of WO<sub>3</sub> nanotubes functionalized with bio-inspired Pd catalysts and their superior hydrogen sensing performance†

Seon-Jin Choi,<sup>a</sup> Saptarshi Chattopadhyay,<sup>b</sup> Jae Jin Kim,<sup>c</sup> Sang-Joon Kim,<sup>a</sup> Harry L. Tuller,<sup>c</sup> Gregory C. Rutledge\*<sup>b</sup> and Il-Doo Kim\*<sup>a</sup>

Macroporous WO<sub>3</sub> nanotubes (NTs) functionalized with nanoscale catalysts were fabricated using coaxial electrospinning combined with sacrificial templating and protein-encapsulated catalysts. The macroporous thin-walled nanotubular structures were obtained by introducing colloidal polystyrene (PS) particles to a shell solution of W precursor and poly(vinylpyrrolidone). After coaxial electrospinning with a core liquid of mineral oil and subsequent calcination, open pores with an average diameter of 173 nm were formed on the surface of WO<sub>3</sub> NTs due to decomposition of the PS colloids. In addition, catalytic Pd nanoparticles (NPs) were synthesized using bio-inspired protein cages, *i.e.*, apoferritin, and uniformly dispersed within the shell solution and subsequently on the WO<sub>3</sub> NTs. The resulting Pd functionalized macroporous WO<sub>3</sub> NTs were demonstrated to be high performance hydrogen (H<sub>2</sub>) sensors. In particular, Pd-functionalized macroporous WO<sub>3</sub> NTs exhibited a very high H<sub>2</sub> response ( $R_{\text{air}}/R_{\text{gas}}$ ) of 17.6 at 500 ppm with a short response time. Furthermore, the NTs were shown to be highly selective for H<sub>2</sub> compared to other gases such as carbon monoxide (CO), ammonia (NH<sub>3</sub>), and methane (CH<sub>4</sub>). The results demonstrate a new synthetic method to prepare highly porous nanotubular structures with well-dispersed nanoscale catalysts, which can provide improved microstructures for chemical sensing.

Received 24th September 2015,  
Accepted 7th December 2015

DOI: 10.1039/c5nr06611e

www.rsc.org/nanoscale

## Introduction

Hydrogen (H<sub>2</sub>) has been regarded as a next generation fuel considering its abundance and high heat of combustion (142 kJ g<sup>-1</sup>).<sup>1,2</sup> In addition, combustion of hydrogen produces only water, without harmful by-products, enabling environmentally friendly energy generation.<sup>3,4</sup> However, there are several potential risks to be addressed prior to commercial use, such as the wide range of flammable concentration (4–75%), low ignition energy (0.02 mJ), high diffusion coefficient (0.61 cm<sup>2</sup> s<sup>-1</sup>), and large flame propagation velocity.<sup>5–7</sup> Moreover, hydrogen gas is colorless, odorless, and tasteless,

which leads to difficulties in detection.<sup>8</sup> For these reasons, a highly sensitive hydrogen detector is required for safe storage and monitoring of hydrogen leakage.

Semiconductor metal oxides (SMOs) have been studied as promising gas sensors, considering their low cost, fast response, stability, and high reactivity toward analyte gases.<sup>9</sup> Recently, advances in nanostructure synthetic methods have promoted the development of highly sensitive and selective gas sensors having a large surface area and porosity.<sup>10,11</sup> Among the various approaches, electrospinning is a facile and versatile method to obtain one-dimensional (1D) SMO nanostructures with a large surface-to-volume ratio and high porosity, adequate for high performance hydrogen sensors.<sup>12,13</sup> A templating route combined with electrospinning has been suggested as a powerful strategy to obtain porous nanostructures.<sup>14</sup> For example, hollow nanotubular structures were demonstrated using electrospun polymeric composite nanofibers (NFs) by coating a thin inorganic layer, such as Al<sub>2</sub>O<sub>3</sub>,<sup>15</sup> NiO,<sup>16</sup> WO<sub>3</sub>,<sup>17,18</sup> and ZnO,<sup>19</sup> and subsequent high-temperature calcination to decompose the inner polymeric component and crystallize the outer inorganic layer. In addition, polymeric colloids were introduced into the electrospinning solution to form pores on SMO NFs.<sup>20–22</sup> It was shown that the pore diameter and distribution on the SMO surface can be controlled by introducing different sizes of the colloid templates.

<sup>a</sup>Department of Material Science and Engineering, Korea Advanced Institute of Science and Technology (KAIST), Daejeon 305-701, Republic of Korea.

E-mail: idkim@kaist.ac.kr; Fax: +82-42-350-5329; Tel: +82-42-350-3329

<sup>b</sup>Department of Chemical Engineering, Massachusetts Institute of Technology, 77 Massachusetts Avenue, Cambridge, MA 02139, USA. E-mail: rutledge@mit.edu; Fax: +1-617-324-3127; Tel: +1-617-253-0171

<sup>c</sup>Department of Materials Science and Engineering, Massachusetts Institute of Technology, 77 Massachusetts Avenue, Cambridge, MA 02139, USA

† Electronic supplementary information (ESI) available: Coaxial electrospinning with different feeding rates, additional TEM analysis for pore size analysis, XPS analysis of Pd-loaded macroporous WO<sub>3</sub> NTs, and dynamic response transition properties of sensors. See DOI: 10.1039/c5nr06611e

Coaxial (or two-fluid) electrospinning has been proposed as an effective method for fabricating hollow nanotubular structures that eliminate additional synthesis processes such as coating of an inorganic layer on the sacrificial templates.<sup>13,23–26</sup> A variety of inorganic nanotubes (NTs) were obtained using coaxial electrospinning, including TiO<sub>2</sub>,<sup>27,28</sup> α-Fe<sub>2</sub>O<sub>3</sub>,<sup>29</sup> and SnO<sub>2</sub><sup>30</sup> for specific applications. However, to the best of our knowledge, coaxial electrospinning combined with sacrificial templating to synthesize macroporous SMO NTs has not yet been demonstrated. The macroporous SMO NTs are advantageous, considering that gas molecules can more effectively diffuse into the core of the SMO NTs, thereby promoting gas reactions on the inner surface.

The catalytic functionalization of SMO-based materials enhances sensitivity and selectivity of gas sensors. Noble metallic nanoparticles (NPs) such as Pt,<sup>31</sup> Pd,<sup>32</sup> and Rh<sup>33,34</sup> are known to be the most effective catalysts for high performance gas sensors. To have a maximum catalytic effect, the diameters of the catalytic NPs should be on the order of a few nanometers.<sup>35</sup> Moreover, a uniform dispersion of the NPs is desirable; otherwise, the sensing performance degrades rapidly due to the agglomeration of catalytic NPs.<sup>36,37</sup>

In this work, we propose a method to fabricate nanocatalyst-loaded macroporous WO<sub>3</sub> NTs using coaxial electrospinning combined with sacrificial templating and bio-inspired catalyst functionalization. Multiple pores were formed on the thin-walled WO<sub>3</sub> NTs after subsequent calcination at high temperature. In addition, a well-dispersed catalyst functionalization was achieved by introducing protein-encapsulated metallic NPs to the shell solution during coaxial electrospinning. The main focus of this research was to examine a new synthetic method to obtain macroporous nanotubular SMO structures with functionalization by well-distributed nanocatalysts, and to demonstrate the remarkably improved hydrogen sensing performances resulting therefrom.

## Experimental section

### Materials

Ammonium metatungstate hydrate [(NH<sub>4</sub>)<sub>6</sub>H<sub>2</sub>W<sub>12</sub>O<sub>40</sub>·xH<sub>2</sub>O], polyvinylpyrrolidone (PVP, *M<sub>w</sub>* = 1 300 000 g mol<sup>-1</sup>), potassium tetrachloropalladate(II) (K<sub>2</sub>PdCl<sub>4</sub>), sodium borohydride (NaBH<sub>4</sub>), heavy mineral oil, and 0.2 μm filtered apoferritin from equine spleen were purchased from Sigma-Aldrich (St Louis, USA). Polystyrene (PS) latex microspheres with the average diameter of 200 nm dispersed at 2.5 wt% in water were purchased from Alfa Aesar (Ward Hill, USA). All chemicals were used without further purification.

### Synthesis of Pd nanoparticles encapsulated by protein cages

To synthesize well-dispersed and nanoscale catalyst particles, we employed bio-inspired protein cages, *i.e.*, apoferritin, that consists of a 24-subunit protein complex with a hollow spherical structure (Fig. 1a). These protein cages can encapsulate metal ions, and the subsequent reduction process can produce

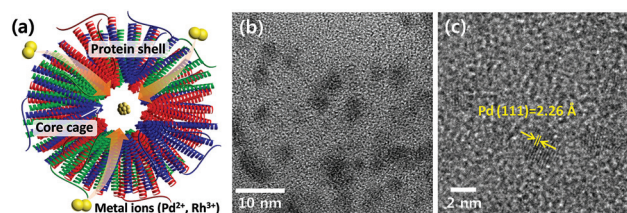


**Fig. 1** (a) Schematic illustration of the apoferritin protein cage for nanocatalyst synthesis. TEM image of (b) apoferritin-encapsulated Pd nanoparticles (AF-Pd NPs), and (c) high-resolution TEM (HR-TEM) image of AF-Pd NPs.

protein-encapsulated metallic NPs.<sup>38</sup> Firstly, 1 g of the apoferritin solution was mixed with 0.1 M NaOH solution to control the pH of the solution at around 8.6. Then, 1.8 wt% of Pd precursor (K<sub>2</sub>PdCl<sub>4</sub>) aqueous solution was added to the apoferritin solution and gently stirred at 100 rpm using a magnetic bar to penetrate Pd<sup>2+</sup> ions into the inner cavity of apoferritin. After stirring for 1 h, a reducing agent of NaBH<sub>4</sub> (1 M) was rapidly injected into the solution to form metallic Pd NPs encapsulated by apoferritin (hereafter, apoferritin-encapsulated Pd NPs are referred to as AF-Pd NPs). Finally, the prepared AF-Pd NPs were centrifuged at 12 000 rpm for 10 min to remove the remaining Pd<sup>2+</sup>, and subsequently re-dispersed in DI water.

### Synthesis of Pd-loaded macroporous WO<sub>3</sub> NTs

Hollow WO<sub>3</sub> nanotubular structures were synthesized by the coaxial electrospinning approach as illustrated in Fig. 2a. Different electrospinning solutions were ejected through the coaxial nozzle (SKU BCN-0802, Inovenso™) having different diameters, *i.e.*, core diameter of 0.8 mm and shell diameter of 1.6 mm, with a concentric configuration. Mineral oil was utilized as a core electrospinning solution due to its easy vaporization at high-temperature. For the shell solution, 0.2 g of ammonium metatungstate hydrate and 0.25 g of PVP were dissolved in 1.5 g of DI water containing 2.5 wt% PS colloids and continuously stirred at room temperature for 3 h. For catalyst functionalization, the prepared AF-Pd NPs were separately introduced in the shell electrospinning solution with a concentration of 0.1 wt%.

Syringes were used to pump the resulting solutions at feeding rates of 10 μL min<sup>-1</sup> and 30–100 μL min<sup>-1</sup> for the mineral oil for the core, and the composite solution for the shell, respectively. A constant DC voltage of 30 kV was applied between the coaxial nozzle and aluminum foil, employed as a collector. The distance between the nozzle and the collector was 15 cm. The as-spun core/shell composite NFs were obtained after coaxial electrospinning (Fig. 2b). The shell layer comprised AF-Pd NPs and W precursor/PVP composites decorated with PS colloids. For the core fluid, mineral oil was used. The as-spun core/shell composite NFs were calcined at 600 °C for 1 h in ambient air to obtain Pd-loaded macroporous WO<sub>3</sub> NTs having multiple, approximately circular pores on the

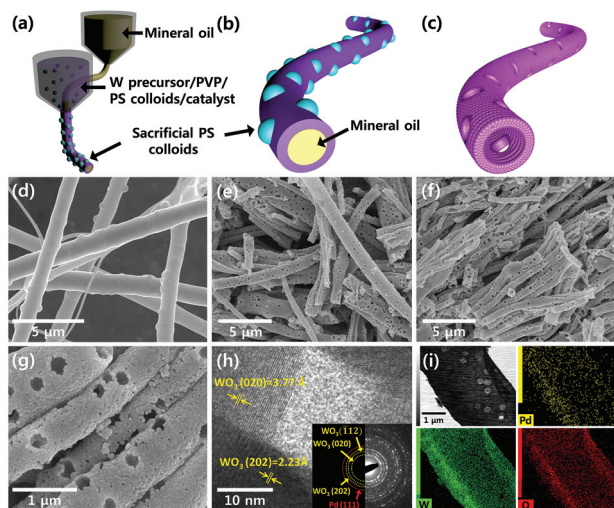


**Fig. 2** Schematic illustrations of (a) coaxial electrospinning using mineral oil in the core and composite solution in the shell, (b) as-spun W precursor/PVP composite nanotubes (NTs) decorated with PS colloid templates and apoferritin-encapsulated nanocatalysts, and (c) catalyst-loaded macroporous  $\text{WO}_3$  NTs with multiple pores after calcination at  $600\text{ }^\circ\text{C}$  for 1 h. SEM images of (d) as-spun W precursor/PVP composite NTs decorated with PS colloid templates, (e) macroporous  $\text{WO}_3$  NTs, (f) Pd-loaded macroporous  $\text{WO}_3$  NTs, and (g) magnified SEM image of (f) after calcination. (h) HR-TEM image with a selected area electron diffraction (SAED) pattern in the inset and (i) scanning TEM image with energy dispersive X-ray spectroscopy (EDS) mapping images of Pd-loaded macroporous  $\text{WO}_3$  NTs.

thin wall of NTs (Fig. 2c). Dense  $\text{WO}_3$  NTs without PS colloid templates and pristine macroporous  $\text{WO}_3$  NTs without catalyst functionalization were synthesized as well, for comparison.

### Characterization of $\text{H}_2$ sensing performances

All of the sensors were stabilized in air for 24 h as a baseline before measurement. The sensors were exposed to different analytes (hydrogen, carbon monoxide, ammonia, and methane) with concentrations ranging from 10 ppm to 500 ppm. Each analyte was exposed for 10 min, followed by 10 min of exposure to air to recover the initial baseline values. The resistance changes were measured using a data acquisition system (34970A, Hewlett-Packard), and the sensors were characterized by their relative response ( $R_{\text{air}}/R_{\text{gas}}$ ), where  $R_{\text{air}}$  is the baseline resistance of the sensor upon exposure to air and  $R_{\text{gas}}$  is the resistance measured upon exposure to a particular analyte. The operating temperature of  $450\text{ }^\circ\text{C}$  for the sensors was controlled within a tubular furnace.

## Results and discussion

### Morphological and structural evaluation

The microstructures of the protein-encapsulated catalytic Pd NPs were examined using TEM (Fig. 1b and c). The good

dispersion of the NPs can be explained by electrostatic repulsion between the protein templates associated with their surface charges. In addition, the overall size of the protein cage was 12–13 nm, whereas the inner cavity size was 7–8 nm.<sup>39</sup> The inner cavity size limited the size of the nanoscale particles to diameters less than 8 nm. As confirmed by TEM analysis, the synthesized AF-Pd NPs showed average diameters of 2 nm (Fig. 1b). Moreover, the Pd NPs were observed to be crystalline, with the crystal planes of Pd (111) corresponding to the inter-planar distances of  $2.26\text{ \AA}$  (Fig. 1c).

The AF-Pd NPs were dispersed in the shell electrospinning solutions for the catalytic functionalization. Core/shell composite NFs decorated with PS colloid templates and apoferritin-encapsulated catalytic NPs were achieved after electrospinning (Fig. 2b). Polymeric components, mineral oil, and protein cages were decomposed during subsequent calcination of the as-spun core/shell composite NFs, while forming  $\text{WO}_3$  NTs by oxidation of the W precursor (Fig. 2c). SEM observations revealed the rugged surface morphology of the as-spun core/shell composite NFs due to the decoration of PS colloids on the surface (Fig. 2d). Different microstructures were obtained after calcination at  $600\text{ }^\circ\text{C}$ , depending on the feeding rate of the shell solution ( $f_s$ ) with the fixed core solution feeding rate ( $f_c = 10\text{ }\mu\text{L min}^{-1}$ ) (ESI, Fig. S1†). When the shell feeding rate was low, *i.e.*,  $f_s = 30\text{ }\mu\text{L min}^{-1}$ , an open tubular structure was formed due to the limited coating of the shell composite solution on mineral oil. On the other hand, perfect tubular structures were achieved when  $f_s$  was  $80\text{ }\mu\text{L min}^{-1}$  or  $100\text{ }\mu\text{L min}^{-1}$ . Fig. 2e shows the macroporous  $\text{WO}_3$  NTs with multiple pores on the surface when  $f_s$  and  $f_c$  were  $100\text{ }\mu\text{L min}^{-1}$  and  $10\text{ }\mu\text{L min}^{-1}$ , respectively. The pore sizes were evaluated by TEM, and the average diameter was  $173\text{ nm}$  (ESI, Fig. S2†). The decreased average pore diameter as compared with the original diameter (*i.e.*,  $200\text{ nm}$ ) of the PS colloid was mainly attributed to the shrinkage of the spherical PS colloids during the thermal decomposition and the migration of the W precursor in the early stage of heat treatment.<sup>20</sup>

The microstructures of the catalytic Pd-loaded macroporous  $\text{WO}_3$  NTs were investigated (Fig. 2f). The surface morphologies of the Pd-loaded macroporous  $\text{WO}_3$  NTs were maintained, with only minor differences when compared to the pristine macroporous  $\text{WO}_3$  NTs. In addition, a close observation of Pd-loaded macroporous  $\text{WO}_3$  NTs exhibited approximately circular pores on the surface (Fig. 2g). The high-resolution TEM (HR-TEM) observation of Pd-loaded macroporous  $\text{WO}_3$  NTs revealed the polycrystalline  $\text{WO}_3$  structures with crystal planes of (020) and (202), which correspond to inter-planar distances of  $3.77\text{ \AA}$  and  $2.23\text{ \AA}$  (Fig. 2h). The selected area electron diffraction (SAED) patterns of Pd-loaded macroporous  $\text{WO}_3$  NTs showed  $\text{WO}_3(020)$ ,  $\text{WO}_3(\bar{1}12)$ , and  $\text{WO}_3(202)$  crystal planes, with inter-planar distances of  $3.77\text{ \AA}$ ,  $3.12\text{ \AA}$ , and  $2.62\text{ \AA}$ , respectively, which are partially investigated in HR-TEM analysis (in the inset of Fig. 2h). However, the crystal planes and SAED patterns of Pd NPs were not clearly observed due to the low content of Pd in the  $\text{WO}_3$  NTs.

To confirm the Pd component and the distribution, energy dispersive X-ray spectroscopy (EDS) analysis was carried out. The result clearly revealed a uniform distribution of Pd over the WO<sub>3</sub> NTs (Fig. 2i). In addition, a scanning TEM image also showed the hollow structure of the Pd-loaded macroporous WO<sub>3</sub> NTs (Fig. 2i). To further confirm the chemical state of Pd, X-ray photoelectron spectroscopy (XPS) analysis was performed (Fig. S3†). Even though the intensities of the Pd peaks were very weak due to the low concentration of Pd in the WO<sub>3</sub> NTs, high-resolution XPS peaks in the vicinity of Pd 3d mainly originated from the oxidized state of Pd, *i.e.*, Pd<sup>2+</sup>(PdO) with binding energies of 336.9 eV and 342.2 eV for 3d<sub>5/2</sub> and 3d<sub>3/2</sub>, respectively.<sup>40</sup>

### Hydrogen gas sensing characterization

To demonstrate the superior H<sub>2</sub> sensing performance of the Pd-loaded macroporous WO<sub>3</sub> NTs, gas sensing characteristics were evaluated using dense WO<sub>3</sub> NTs, macroporous WO<sub>3</sub> NTs (porous WO<sub>3</sub> NTs), and Pd-loaded macroporous WO<sub>3</sub> NTs (Pd-porous WO<sub>3</sub> NTs) in the concentration range of 10–500 ppm at 450 °C (Fig. 3). Dynamic sensor response measurements showed that an approximately 1.6-fold improvement in the H<sub>2</sub> response was observed with the porous WO<sub>3</sub> NTs ( $R_{\text{air}}/R_{\text{gas}} = 4.9$ ) compared to the response of dense WO<sub>3</sub> NTs ( $R_{\text{air}}/R_{\text{gas}} = 3$ ). In addition, a dramatically improved H<sub>2</sub> response of 17.6 was obtained with Pd-porous WO<sub>3</sub> NTs at 500 ppm, which was 5.9- and 3.6-fold better than those observed with dense WO<sub>3</sub>

NTs and porous WO<sub>3</sub> NTs, respectively. Furthermore, Pd-porous WO<sub>3</sub> NTs exhibited an outstanding response ( $R_{\text{air}}/R_{\text{gas}} = 2.6$ ) at a very low concentration of 10 ppm (ESI, Fig. S4†).

The response time characteristics of the sensors were investigated at different concentrations (Fig. 3b). The response time is defined as the elapsed time to reach 90% of the saturated maximum response. The Pd-loaded macroporous WO<sub>3</sub> NTs showed a fast response due to catalytically enhanced surface reactions. A very fast response within 25 s was achieved with Pd-porous WO<sub>3</sub> NTs at 500 ppm of H<sub>2</sub>. However, relatively slow response times with dense WO<sub>3</sub> NTs (35 s) and porous WO<sub>3</sub> NTs (50 s) were observed at the same concentration. In particular, the porous WO<sub>3</sub> NTs showed much longer response times than the dense WO<sub>3</sub> NTs. This can be attributed to the fact that the porous WO<sub>3</sub> NTs had more available surface reaction sites as a result of the formation of open pores, which accounted for the longer response time as well as the slightly improved response compared to the dense WO<sub>3</sub> NTs. In addition, it should be noted that all the sensors showed longer response times at low H<sub>2</sub> concentration. The observation of longer response times with decreasing gas concentrations has been reported previously.<sup>41–43</sup> This can be attributed to diffusion-limited kinetics at low H<sub>2</sub> concentration. Based on theoretical considerations, the response time can be explained by a non-linear diffusion reaction model.<sup>44</sup> In that study, the diffusion time ( $\tau$ ) was defined by

$$\tau = kx_0^2 C_0^{r-1} / D \quad (1)$$

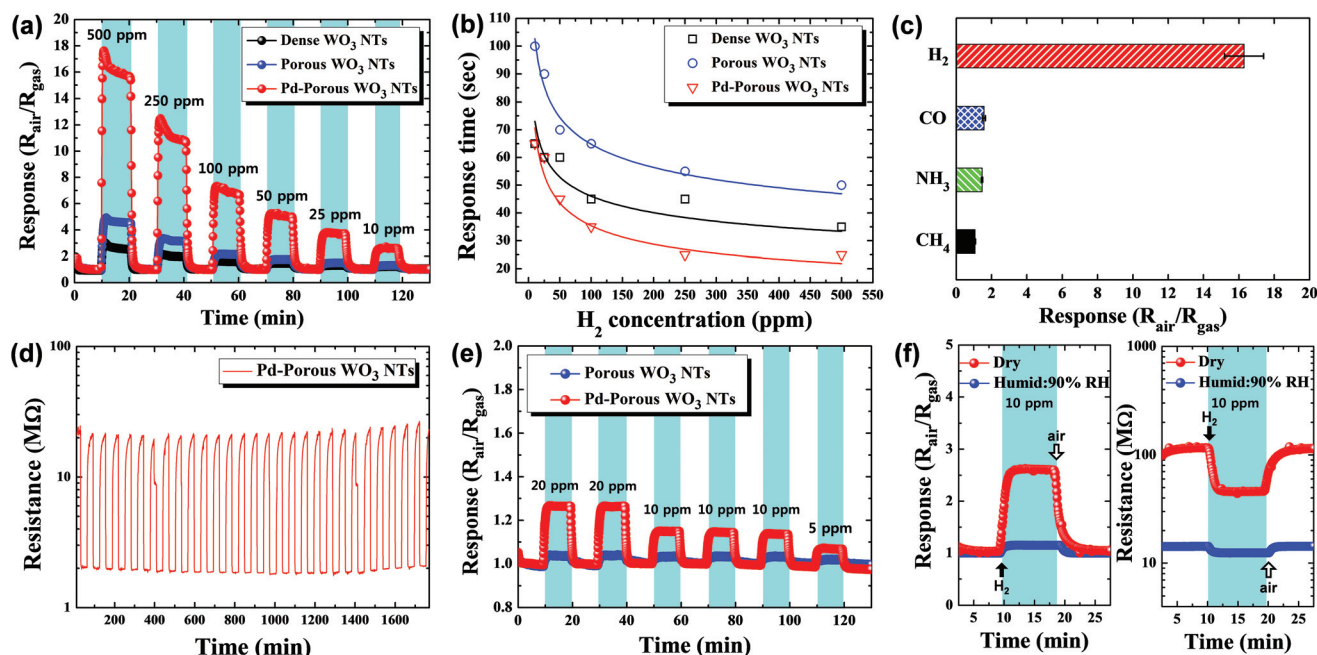


**Fig. 3** (a) Dynamic signal response and (b) response times of dense WO<sub>3</sub> NTs, porous WO<sub>3</sub> NTs, and Pd-porous WO<sub>3</sub> NTs in the gas concentration range of 10–500 ppm. (c) Selective H<sub>2</sub> sensing property of Pd-porous WO<sub>3</sub> NTs against other analytes with a gas concentration of 500 ppm. (d) Cyclic resistance response of Pd-porous WO<sub>3</sub> NTs toward H<sub>2</sub> with a gas concentration of 500 ppm. (e) Dynamic response of porous WO<sub>3</sub> NTs and Pd-porous WO<sub>3</sub> NTs in the gas concentration range of 5–20 ppm in air at high relative humidity (90% RH). (f) Dynamic signal and resistance response of Pd-porous WO<sub>3</sub> NTs to 10 ppm of H<sub>2</sub> in dry and humid air. All measurements were performed at 450 °C.

where,  $k$ ,  $x_0$ ,  $C_0$ , and  $D$  are the reaction rate constant, film thickness, gas concentration, and diffusion coefficient, respectively. The constant  $r$  was found to be in the range of 0.3–1. In the present study, our sensor exhibited a value for  $r$  in the range of 0.7–0.8 as indicated by fitting of eqn (1) to the data in Fig. 3b. The model is based on the dependence of response time on gas concentration. Specifically, the response time is determined by a non-linear adsorption isotherm, which leads to a concentration-dependent response time.

The selectivity of H<sub>2</sub> detection with respect to other potentially interfering gases such as carbon monoxide (CO), ammonia (NH<sub>3</sub>), and methane (CH<sub>4</sub>) at 500 ppm was investigated using Pd-porous WO<sub>3</sub> NTs (Fig. 3c). The results revealed that Pd-porous WO<sub>3</sub> NTs showed a remarkably high H<sub>2</sub> response ( $R_{\text{air}}/R_{\text{gas}} = 16.3 \pm 1.1$ ) with a weak response ( $R_{\text{air}}/R_{\text{gas}} < 1.6$ ) toward the other gases, confirming the high H<sub>2</sub> selectivity of these materials. The stable H<sub>2</sub> sensing properties of Pd-porous WO<sub>3</sub> NTs were evaluated as well by cyclic exposure of H<sub>2</sub> (Fig. 3d). The sensor showed stable resistance changes over 25 cycles toward 500 ppm of H<sub>2</sub>.

The effect of moisture on the response to H<sub>2</sub> was investigated using the porous WO<sub>3</sub> NTs and Pd-porous WO<sub>3</sub> NTs in the concentration range of 5–20 ppm in air with high relative humidity (90% RH) at 450 °C (Fig. 3e). Under these conditions, the Pd-porous WO<sub>3</sub> NTs exhibited a response of 1.26 at 20 ppm, which is a 20% improvement in response compared to that of pristine porous WO<sub>3</sub> NTs. However, dramatically decreased response characteristics were observed in both Pd-porous WO<sub>3</sub> NTs and pristine porous WO<sub>3</sub> NTs under the high humidity conditions. A reduction in the response of approximately 90% was observed for Pd-porous WO<sub>3</sub> NTs at 10 ppm of H<sub>2</sub> in humid air (Fig. 3f). The relatively insensitive H<sub>2</sub> response of Pd-porous WO<sub>3</sub> NTs in humid air is mainly attributed to the formation of hydroxyl groups (–OH) on the surface of WO<sub>3</sub> NTs.<sup>45</sup> As a result, decreased baseline resistance was also observed with Pd-porous WO<sub>3</sub> NTs in humid air (Fig. 3f).

### Hydrogen sensing mechanism

The mechanism responsible for the improved H<sub>2</sub> sensing performance of the Pd-porous WO<sub>3</sub> NTs was investigated (Fig. 4). The changes in the dynamic resistance of the sensors with respect to changes in H<sub>2</sub> concentrations were evaluated by comparing the baseline resistances and resistance changes (Fig. 4a). All the sensors exhibited decreasing resistance when the sensors were exposed to H<sub>2</sub> gas. This decrease is normally attributed to the elimination of chemisorbed oxygen species, *i.e.*, O<sup>–</sup>, O<sup>2–</sup>, and O<sub>2</sub><sup>–</sup>, by their reaction with H<sub>2</sub> on the surface of WO<sub>3</sub>. When an n-type WO<sub>3</sub> is stabilized in ambient air, oxygen species are chemisorbed on the surface of WO<sub>3</sub>, withdrawing electrons from the conduction band to provide the baseline resistance. Then, upon exposure to H<sub>2</sub> gas, the resistance decreases as H<sub>2</sub> reacts with the chemisorbed oxygen species, thereby donating electrons back to the conduction band of the WO<sub>3</sub>.

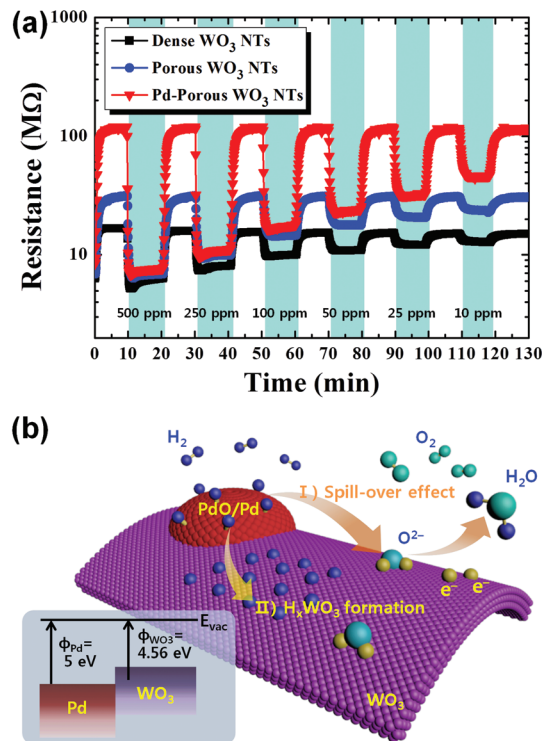


Fig. 4 (a) Dynamic resistance changes of dense WO<sub>3</sub> NTs, porous WO<sub>3</sub> NTs, and Pd-porous WO<sub>3</sub> NTs toward H<sub>2</sub> within the concentration range of 10–500 ppm at 450 °C. (b) Schematic illustration of H<sub>2</sub> sensing mechanism of Pd-porous WO<sub>3</sub> NTs.

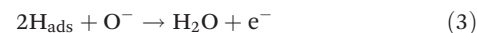
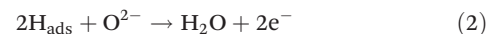
Comparing the baseline resistances, pristine porous WO<sub>3</sub> NTs exhibited a slightly higher resistance (31.5 MΩ) than that of dense WO<sub>3</sub> NTs (16.7 MΩ), which was mainly attributed to the macroporous structure of the former. In the case of Pd-porous WO<sub>3</sub> NTs, there was a huge increase in the baseline resistance (119.9 MΩ) compared to the other sensors. The increased baseline resistance can be explained by the formation of a Schottky barrier between Pd and WO<sub>3</sub> (Fig. 4b). The different work functions of Pd ( $\phi = 5$  eV)<sup>46</sup> and WO<sub>3</sub> ( $\phi = 4.56$  eV)<sup>20</sup> can form an electron depletion layer at the interface, which results in the increase in baseline resistance. In addition, the formation of a p–n junction can increase the baseline resistance. In other words, Pd can be slightly oxidized to form a p-type PdO on the surface of Pd due to the high-temperature calcination in ambient air.<sup>32</sup> The formation of a p–n junction can also expand the electron depletion layer at the interface, thereby increasing the baseline resistance.

The reaction mechanisms responsible for the large resistance changes of Pd-porous WO<sub>3</sub> NTs toward H<sub>2</sub> are discussed next. As shown in the schematic illustration in Fig. 4b, two reactions are mainly affected by catalytic Pd. Generally, Pd can dissociate H<sub>2</sub> molecules into H atoms (H<sub>ads</sub>) on the surface of Pd NP. These H atoms are distributed onto the WO<sub>3</sub> surface, which is known as the ‘spill-over effect’, to react with chemi-

Table 1 Comparison of important parameters for H<sub>2</sub> sensors

Composites	Sensing type	Response definition	Sensitivity (response)	Detection limit	Selectivity	Response/recovery time	Operating temp.	Ref.
Pd-WO <sub>3</sub> nanotubes	Resistivity	$R_{\text{air}}/R_{\text{gas}}$	17.6@500 ppm	10 ppm	CH <sub>4</sub> , CO, NH <sub>3</sub>	25 s/—	450 °C	This work
Pd-WO <sub>3</sub> nanoplates	Resistivity	$R_{\text{air}}/R_{\text{gas}}$	843@0.3 vol%	0.1 vol%	CH <sub>4</sub> , C <sub>3</sub> H <sub>6</sub> O, C <sub>2</sub> H <sub>6</sub> , C <sub>3</sub> H <sub>8</sub> O, NH <sub>3</sub>	~50 s/~/25 s	80 °C	47
Pd-WO <sub>3</sub> nanoplates	Conductivity	$R_{\text{air}}/R_{\text{gas}}$	34@0.1 vol%	0.05%	—	24 s/—	Room Temp.	48
Pd-WO <sub>3</sub> nanolamellae	Resistivity	$R_{\text{air}}/R_{\text{gas}}$	~6 × 10 <sup>3</sup> @400 ppm	200 ppm	—	—/—	250 °C	49
Pd/WO <sub>3</sub> films	Resistivity	$(R_0 - R_{\text{H}_2})/R_{\text{H}_2}$	4.77 × 10 <sup>4</sup> @2%	500 ppm	—	—/47 s	80 °C	50
Pd-WO <sub>3</sub> thick films	Resistivity	$(R_{\text{air}} - R_{\text{gas}})/R_{\text{gas}}$	69@200 ppm	50 ppm	—	<5 min/—	180 °C	51
Pd-WO <sub>3</sub> nanowires	Resistivity	$R_{\text{air}}/R_{\text{gas}}$	3.1@1000 ppm	1000 ppm	C <sub>3</sub> H <sub>6</sub> O, CH <sub>4</sub> O, C <sub>3</sub> H <sub>8</sub> O	76 s/2491 s	300 °C	52
Pd-WO <sub>3</sub> films (Pd/W = 10%)	Voltage change	$(V_{\text{gas}} - V_{\text{air}})/V_{\text{air}}$	2.5 × 10 <sup>4</sup> @1300 ppm	1300 ppm	—	~100 s/~/4000 s	Room Temp.	53
Pd-WO <sub>3</sub> films	Conductivity	$(I_{\text{gas}}/I_{\text{air}}) - 1$	400@2300 ppm	2300 ppm	CH <sub>4</sub>	102 s/7 s	350 °C	54
Pd-WO <sub>3</sub> films	Resistivity	$(R_0 - R_{\text{H}_2})/R_{\text{H}_2}$	1200@3000 ppm	4 ppm	CH <sub>4</sub> O, C <sub>2</sub> H <sub>6</sub> O, C <sub>3</sub> H <sub>6</sub> O, C <sub>3</sub> H <sub>8</sub> O, CH <sub>2</sub> O	1400 s/—	Room Temp.	55
Pd-WO <sub>3</sub> nanowires	Conductivity	$(G - G_0)/(G_0 \times 100\%)$	~1000@1000 ppm	10 ppm	NO, H <sub>2</sub> S, CO	—/~/900 s	130 °C	56

sorbed oxygen species (*i.e.*, O<sup>2-</sup> and O<sup>-</sup>), resulting in the production of H<sub>2</sub>O molecules as expressed in the following reactions.<sup>57,58</sup>



The other reaction path is the formation of hydrogen tungsten bronzes (H<sub>x</sub>WO<sub>3</sub>) on the surface of WO<sub>3</sub> NTs by the partial reduction of WO<sub>3</sub>, as described below.<sup>47</sup>



The hydrogen atoms serve as electron donors, thereby increasing the free carriers in WO<sub>3</sub> and decreasing the overall resistance of Pd-porous WO<sub>3</sub> NTs.<sup>48</sup> Therefore, these two reaction paths are believed to be responsible for the large decrease in resistance from the baseline, and for the strong response of Pd-porous WO<sub>3</sub> NTs toward H<sub>2</sub>.

Pd-WO<sub>3</sub> composites have been demonstrated to be outstanding sensing materials for H<sub>2</sub> detection. Table 1 summarizes recent publications on Pd-WO<sub>3</sub> composite sensing layers for H<sub>2</sub> detection. A majority of the previous studies were performed using thin film structures, whereas a few studies demonstrate the superior H<sub>2</sub> sensing properties using nanostructures. Regardless, the present work shows a relatively strong response ( $R_{\text{air}}/R_{\text{gas}} = 17.6$ ) at relatively low H<sub>2</sub> concentrations, compared to the previous studies. In addition, we demonstrated the lowest limit of detection (10 ppm) with a very fast response time (25 s).

## Conclusions

In this work, we have demonstrated the use of coaxial electrospinning combined with sacrificial templating to produce macroporous semiconductor metal oxide (SMO) nanostructures. During the coaxial electrospinning, PS colloids were introduced to the electrospinning solution to serve as templates for the macropores on the surface of the WO<sub>3</sub> NTs. Circular-shaped pores with an average diameter of 173 nm were achieved on the WO<sub>3</sub> NTs after subsequent calcination. The apoferritin protein cage is shown to be a powerful agent for distributing nanocatalyst uniformly on SMO sensing layers. The noble metallic Pd NPs were synthesized using apoferritin protein cages and thus distributed on the macroporous WO<sub>3</sub> NTs during coaxial electrospinning. The Pd-loaded macroporous WO<sub>3</sub> NTs exhibited very fast response times, which is mainly attributed to the catalytic effect of Pd. In particular, Pd-loaded macroporous WO<sub>3</sub> NTs showed high sensitivity and selectivity toward H<sub>2</sub>. A high response ( $R_{\text{air}}/R_{\text{gas}}$ ) of 17.6 was achieved for 500 ppm of H<sub>2</sub>. In addition, Pd-loaded macroporous WO<sub>3</sub> NTs revealed high H<sub>2</sub> selectivity with a weak response toward potential interfering gases such as CO, NH<sub>3</sub>, and CH<sub>4</sub>. This work provides a novel synthetic method using two-fluid electrospinning for macroporous WO<sub>3</sub> NTs with bio-inspired nanocatalysts for high performance chemical sensors.

## Acknowledgements

This work was supported by the Center for Integrated Smart Sensors funded by the Ministry of Science, ICT & Future Planning as a Global Frontier Project (CISS-2011-0031870) and partially funded by Intel's University Research Office (URO). This work was also supported by the Ministry of Science, ICT & Future Planning as Biomedical Treatment Technology Development Project (2015M3A9D7067418). We also would like to acknowledge the Institute for Soldier Nanotechnologies at MIT for use of facilities. HLT acknowledges support by the MRSEC Program of the National Science Foundation under award number DMR – 1419807.

## Notes and references

- P. A. Russo, N. Donato, S. G. Leonardi, S. Baek, D. E. Conte, G. Neri and N. Pinna, *Angew. Chem., Int. Ed.*, 2012, **51**, 11053–11057.
- T. Hubert, L. Boon-Brett, G. Black and U. Banach, *Sens. Actuators, B*, 2011, **157**, 329–352.
- M. Z. Ahmad, V. B. Golovko, R. H. Adnan, F. Abu Bakar, J. Y. Ruzicka, D. P. Anderson, G. G. Andersson and W. Wlodarski, *Int. J. Hydrogen Energy*, 2013, **38**, 12865–12877.
- S. K. Arya, S. Krishnan, H. Silva, S. Jean and S. Bhansali, *Analyst*, 2012, **137**, 2743–2756.
- N. H. Al-Hardan, M. J. Abdullah and A. A. Aziz, *Int. J. Hydrogen Energy*, 2010, **35**, 4428–4434.
- E. Sennik, Z. Colak, N. Kilinc and Z. Z. Ozturk, *Int. J. Hydrogen Energy*, 2010, **35**, 4420–4427.
- S. Sumida, S. Okazaki, S. Asakura, H. Nakagawa, H. Murayama and T. Hasegawa, *Sens. Actuators, B*, 2005, **108**, 508–514.
- T. Samerjai, N. Tamaekong, C. Liewhiran, A. Wisitsoraat, A. Tuantranont and S. Phanichphant, *Sens. Actuators, B*, 2011, **157**, 290–297.
- I. D. Kim, A. Rothschild and H. L. Tuller, *Acta Mater.*, 2013, **61**, 974–1000.
- T. Wagner, S. Haffer, C. Weinberger, D. Klaus and M. Tiemann, *Chem. Soc. Rev.*, 2013, **42**, 4036–4053.
- D. J. Wales, J. Grand, V. P. Ting, R. D. Burke, K. J. Edler, C. R. Bowen, S. Mintova and A. D. Burrows, *Chem. Soc. Rev.*, 2015, **44**, 4290–4321.
- B. Ding, M. R. Wang, X. F. Wang, J. Y. Yu and G. Sun, *Mater. Today*, 2010, **13**, 16–27.
- A. Greiner and J. H. Wendorff, *Angew. Chem., Int. Ed.*, 2007, **46**, 5670–5703.
- H. Y. Chen, J. C. Di, N. Wang, H. Dong, J. Wu, Y. Zhao, J. H. Yu and L. Jiang, *Small*, 2011, **7**, 1779–1783.
- Q. Peng, X. Y. Sun, J. C. Spagnola, G. K. Hyde, R. J. Spontak and G. N. Parsons, *Nano Lett.*, 2007, **7**, 719–722.
- N. G. Cho, H. S. Woo, J. H. Lee and I. D. Kim, *Chem. Commun.*, 2011, **47**, 11300–11302.
- S. J. Choi, F. Fuchs, R. Demadrille, B. Grevin, B. H. Jang, S. J. Lee, J. H. Lee, H. L. Tuller and I. D. Kim, *ACS Appl. Mater. Interfaces*, 2014, **6**, 9061–9070.
- S. J. Choi, I. Lee, B. H. Jang, D. Y. Youn, W. H. Ryu, C. O. Park and I. D. Kim, *Anal. Chem.*, 2013, **85**, 1792–1796.
- S. H. Choi, G. Ankonina, D. Y. Youn, S. G. Oh, J. M. Hong, A. Rothschild and I. D. Kim, *ACS Nano*, 2009, **3**, 2623–2631.
- S. J. Choi, C. Choi, S. J. Kim, H. J. Cho, M. Hakim, S. Jeon and I. D. Kim, *Sci. Rep.*, 2015, **5**, 8067.
- S. J. Choi, S. J. Kim, W. T. Koo, H. J. Cho and I. D. Kim, *Chem. Commun.*, 2015, **51**, 2609–2612.
- S. J. Choi, C. Choi, S. J. Kim, H. J. Cho, S. Jeon and I. D. Kim, *RSC Adv.*, 2015, **5**, 7584–7588.
- H. L. Qu, S. Y. Wei and Z. H. Guo, *J. Mater. Chem. A*, 2013, **1**, 11513–11528.
- D. Li and Y. N. Xia, *Nano Lett.*, 2004, **4**, 933–938.
- J. H. Yu, S. V. Fridrikh and G. C. Rutledge, *Adv. Mater.*, 2004, **16**, 1562–1566.
- Z. C. Sun, E. Zussman, A. L. Yarin, J. H. Wendorff and A. Greiner, *Adv. Mater.*, 2003, **15**, 1929–1932.
- X. Zhang, V. Aravindan, P. S. Kumar, H. Liu, J. Sundaramurthy, S. Ramakrishna and S. Madhavi, *Nanoscale*, 2013, **5**, 5973–5980.
- X. Zhang, V. Thavasi, S. G. Mhaisalkar and S. Ramakrishna, *Nanoscale*, 2012, **4**, 1707–1716.
- S. Chaudhari and M. Srinivasan, *J. Mater. Chem.*, 2012, **22**, 23049–23056.
- J. Cao, T. Zhang, F. Li, H. Yang and S. Liu, *New J. Chem.*, 2013, **37**, 2031–2036.
- J. Shin, S. J. Choi, I. Lee, D. Y. Youn, C. O. Park, J. H. Lee, H. L. Tuller and I. D. Kim, *Adv. Funct. Mater.*, 2013, **23**, 2357–2367.
- D. J. Yang, I. Kamienchick, D. Y. Youn, A. Rothschild and I. D. Kim, *Adv. Funct. Mater.*, 2010, **20**, 4258–4264.
- K. I. Choi, S. J. Hwang, Z. F. Dai, Y. C. Kang and J. H. Lee, *RSC Adv.*, 2014, **4**, 53130–53136.
- S. J. Kim, I. S. Hwang, C. W. Na, I. D. Kim, Y. C. Kang and J. H. Lee, *J. Mater. Chem.*, 2011, **21**, 18560–18567.
- N. Ma, K. Suematsu, M. Yuasa and K. Shimano, *ACS Appl. Mater. Interfaces*, 2015, **7**, 15618–15625.
- S. Vallejos, T. Stoycheva, P. Umek, C. Navio, R. Snyders, C. Bittencourt, E. Llobet, C. Blackman, S. Moniz and X. Correig, *Chem. Commun.*, 2011, **47**, 565–567.
- I. S. Hwang, J. K. Choi, H. S. Woo, S. J. Kim, S. Y. Jung, T. Y. Seong, I. D. Kim and J. H. Lee, *ACS Appl. Mater. Interfaces*, 2011, **3**, 3140–3145.
- J. Jang, S. Kim, S.-J. Choi, N.-H. Kim, H. Meggie, A. Rothschild and I.-D. Kim, *Nanoscale*, 2015, **7**, 16417–16426.
- Z. Heger, S. Skalickova, O. Zitka, V. Adam and R. Kizek, *Nanomedicine*, 2014, **9**, 2233–2245.
- N. H. Kim, S. J. Choi, D. J. Yang, J. Bae, J. Park and I. D. Kim, *Sens. Actuators, B*, 2014, **193**, 574–581.
- V. N. Mishra and R. P. Agarwal, *Microelectron. J.*, 1998, **29**, 861–874.
- H. R. Kim, K. I. Choi, J. H. Lee and S. A. Akbar, *Sens. Actuators, B*, 2009, **136**, 138–143.



- 43 E. Rossinyol, A. Prim, E. Pellicer, J. Arbiol, F. Hernandez-Ramirez, F. Peiro, A. Cornet, J. R. Morante, L. A. Solovyov, B. Z. Tian, T. Bo and D. Y. Zhao, *Adv. Funct. Mater.*, 2007, **17**, 1801–1806.
- 44 J. W. Gardner, *Sens. Actuators, B*, 1990, **1**, 166–170.
- 45 H. Li, B. Liu, D. P. Cai, Y. R. Wang, Y. Liu, L. Mei, L. L. Wang, D. D. Wang, Q. H. Li and T. H. Wang, *J. Mater. Chem. A*, 2014, **2**, 6854–6862.
- 46 J. H. Ahn, J. Yun, Y. K. Choi and I. Park, *Appl. Phys. Lett.*, 2014, **104**, 013508.
- 47 Y. R. Wang, B. Liu, S. H. Xiao, H. Li, L. L. Wang, D. P. Cai, D. D. Wang, Y. Liu, Q. H. Li and T. H. Wang, *J. Mater. Chem. A*, 2015, **3**, 1317–1324.
- 48 B. Liu, D. P. Cai, Y. Liu, D. D. Wang, L. L. Wang, Y. R. Wang, H. Li, Q. H. Li and T. H. Wang, *Sens. Actuators, B*, 2014, **193**, 28–34.
- 49 Z. Q. Hua, M. Yuasa, T. Kida, N. Yamazoe and K. Shimano, *Thin Solid Films*, 2013, **548**, 677–682.
- 50 M. Zhao, J. Huang and C.-W. Ong, *Int. J. Hydrogen Energy*, 2013, **38**, 15559–15566.
- 51 A. Boudiba, C. Zhang, P. Umek, C. Bittencourt, R. Snyders, M. G. Olivier and M. Debliquy, *Int. J. Hydrogen Energy*, 2013, **38**, 2565–2577.
- 52 F. Chavez, G. F. Perez-Sanchez, O. Goiz, P. Zaca-Moran, R. Pena-Sierra, A. Morales-Acevedo, C. Felipe and M. Soledad-Priego, *Appl. Surf. Sci.*, 2013, **275**, 28–35.
- 53 S. Fardindoost, A. I. Zad, F. Rahimi and R. Ghasempour, *Int. J. Hydrogen Energy*, 2010, **35**, 854–860.
- 54 E. Ghadiri, A. Iraji zad and F. Razi, *Synth. React. Inorg. Met.-Org. Chem.*, 2007, **37**, 453–456.
- 55 M. Zhao, J. X. Huang and C. W. Ong, *Nanotechnology*, 2012, **23**, 315503.
- 56 J. Kukkola, M. Mohl, A. R. Leino, J. Maklin, N. Halonen, A. Shchukarev, Z. Konya, H. Jantunen and K. Kordas, *Sens. Actuators, B*, 2013, **186**, 90–95.
- 57 Z. Y. Zhang, X. M. Zou, L. Xu, L. Liao, W. Liu, J. Ho, X. H. Xiao, C. Z. Jiang and J. C. Li, *Nanoscale*, 2015, **7**, 10078–10084.
- 58 X. W. Li, Y. Liu, J. C. Hemminger and R. M. Penner, *ACS Nano*, 2015, **9**, 3215–3225.